

Future Dynamics of the Local Group. I. MW-M31 Interactions

COLIN LEACH 

ABSTRACT

TODO Add a concise and intelligent summary of the paper, once I get a clearer idea what it will include (and how to seem intelligent).

Keywords: Galaxy Merger – Local Group – Stellar Disk – Stellar Bulge – Dark Matter Halo – Hernquist Profile – Merger Remnant

1. INTRODUCTION

The currently-accepted model of galaxy formation involves baryonic matter (gas and dust) falling into gravitational potential wells created by local over-densities in the Dark Matter (DM). Further gravitational collapse and Jeans fragmentation can then lead to creation of galaxies and stars (Mo et al. 2010).

However, decades of observational and theoretical studies tell us that, firstly, this by itself does not account for the wide range of galaxy morphologies seen at all epochs; secondly, there is no reason to suppose that galaxies continue in serene isolation after their formation.

Attempts to model interactions and mergers between galaxies with numerical simulations goes back at least to Toomre & Toomre (1972). This field continues to develop, with improvements in both hardware and algorithms allowing larger particle numbers in N-body simulations **TODO** refs? and more sophisticated treatment of gas hydrodynamics, magnetic fields and other factors.

As with all theoretical studies, it is vital to stay connected to the best experimental data as this constantly evolves, constantly comparing models against observations. Checking simulations against high-redshift galaxies is necessary but inevitably approximate. A perhaps more rigorous test is to model the galaxies for which we have the most precise and detailed observational measurements: those which are (by far) closest to us.

The largest galaxies in our Local Group (LG) are the Milky Way (MW), Andromeda (M31) and Triangulum (M33). A simulation of MW–M31–M33 orbital evolution was described previously in Marel et al. (2012a), hereafter vdM12. That paper included an extensive analysis of both N-body simulations and semi-analytic orbit integrations. The present study uses data from the same N-body simulation to carry out further computational analysis.

The simulation was based on data in (Marel et al. 2012b) suggesting that M31 is approaching the MW directly with little proper motion detected by Hubble Space Telescope studies. Recent data from Gaia DR2 (Brown et al. 2018) suggest that infall is slightly less radial than previously thought (Marel et al. 2019), leading to a slightly later first approach with a larger pericenter distance. However, detailed simulations based on that new data have not yet been carried out.

This paper will review the initial conditions and time evolution for multiple physical parameters of the simulation. Particular attention will be paid to the first MW-M31 close approach around 4 Gyr, the second approach and merger around 6 Gyr, and the structure and dynamics of the post-merger remnant.

Time probably precludes much analysis of the fate of M33, which will need to be the subject of a future paper.

1.1. Data

Data from one N-body simulation in vdM12 was supplied in text-file format by one of the original authors. This included position and velocity data for each particle at the current epoch ($t = 0$) and 800 future time steps. For ease of analysis, this was all transferred to the open source database PostgreSQL¹ (approximately 1.35 billion records). The same database was used to store computed summary data during the analysis.

Particle counts for each time point are shown in Table 1 and total masses in Table 2. We can see that total mass is the same for MW/M31 but our galaxy has more dark matter (lower baryon fraction) and M31 has more luminous stars (higher baryon fraction). M33 is about 10-fold lighter than either.

The coordinate system is approximately centered on the Milky Way at $t = 0$. The center of mass (CoM) of

¹ <http://www.postgresql.org>

Table 1. Particle counts

Galaxy	DM Halo	Disk	Bulge	Total
MW	250,000	375,000	50,000	675,000
M31	250,000	600,000	95,000	945,000
M33	25,000	46,500	0	71,500
LG	525,000	1,021,500	145,000	1,691,500

Table 2. Aggregate masses ($M_{\odot} \times 10^{12}$)

Galaxy	DM Halo	Disk	Bulge	Total
MW	1.975	0.075	0.010	2.060
M31	1.921	0.120	0.019	2.060
M33	0.187	0.009	0.000	0.196
LG	4.082	0.204	0.029	4.316

all particles in the system is not fixed over time, moving at an average of $\vec{v} = \langle 35.9, -26.7, 27.5 \rangle$ km/s with some minor fluctuations due to numerical approximations. In contrast, the total angular momentum of the system is very small at all time points.

1.2. Software

The work in this report was carried out in Python using standard packages. Full details are available online²

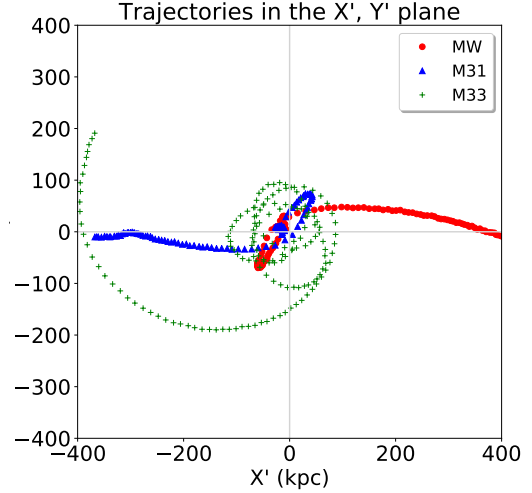
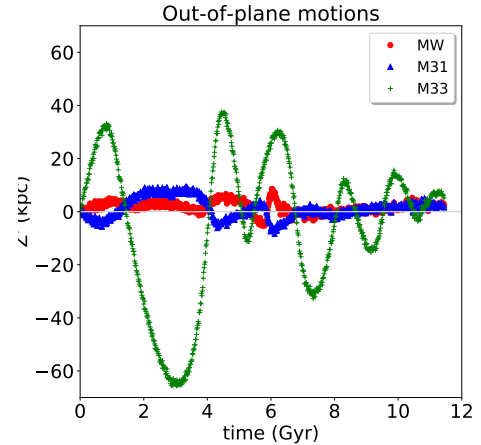
2. RESULTS

2.1. Trajectories

The simulation does not explicitly include a supermassive black hole (SMBH) at the center of each galaxy, but the galactic center was defined by calculating the center of mass (CoM) of the disk particles and iteratively constraining the radius of interest until convergence.

To plot motions of the three galactic CoMs it is convenient to transform to a coordinate system in which at $t = 0$ they all lie in the x, y plane with MW and M31 on the x -axis. The overall CoM is moving, as noted above, so at each time point the coordinates are translated to center it at the origin.

In vdM12 this is referred to as the X', Y', Z' coordinate system and their figure 2 shows multiple views of how the galaxies move through time. In this paper, Fig-

**Figure 1.** Trajectories of each galactic center of mass in the X', Y' plane. Points are at 71 Myr intervals.**Figure 2.** Trajectories of each galactic center of mass perpendicular to the X', Y' plane.

ures 1 and 2 show some alternative views in essentially the same coordinates (up to a sign; the x and z axes are flipped). Figure 1 reproduces the top left panel of vdM12. Figure 2 shows that MW and M31 remain close to the starting plane while M33 has larger, irregular out-of-plane motions.

Relative motions of the CoMs are shown against time in Figures 3 and 4, equivalent to figures 3 and 4 in vdM12.

There is a MW-M31 close approach with first pericenter at 3.96 Gyr with a minimum separation of 35.1 kpc, then a separation to 173 kpc at apocenter and finally a convergence to 7.8 kpc at second pericenter and merger between 5.9 - 6.5 Gyr. Relative velocities spike

² Code https://github.com/colinleach/400B_Leach
documentation <https://400b-leach.readthedocs.io>

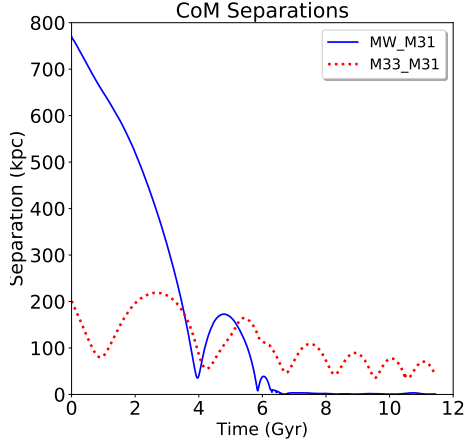


Figure 3. Separations of galactic CoMs.

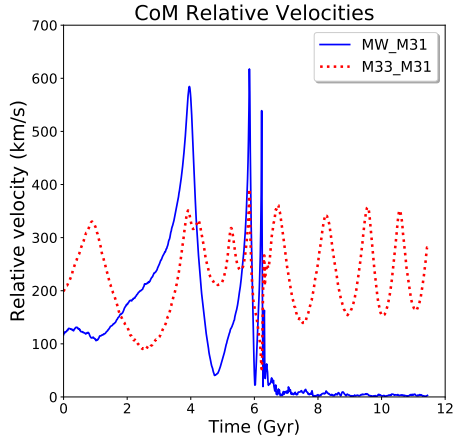


Figure 4. Relative velocities of galactic CoMs.

sharply during these approaches, as potential energy is converted to kinetic energy, before declining to essentially zero.

Meanwhile, in this simulation run M33 remains separate throughout, albeit on a decaying orbit. In vdM12 the authors investigate the effect of small changes in initial conditions and estimate a 9% chance of an M33-MW collision at first pericenter, before the M31-MW merger.

2.2. Mass profiles and rotation curves

Figure 5 shows the cumulative mass profile, by particle type and in total, for each galaxy. The center of each galaxy is dominated by baryonic matter with the DM halo becoming dominant at larger radii.

Figure 6 shows the rotation curves expected from these mass profiles. Without the DM halo the circular velocity would peak within a few kpc of the CoM

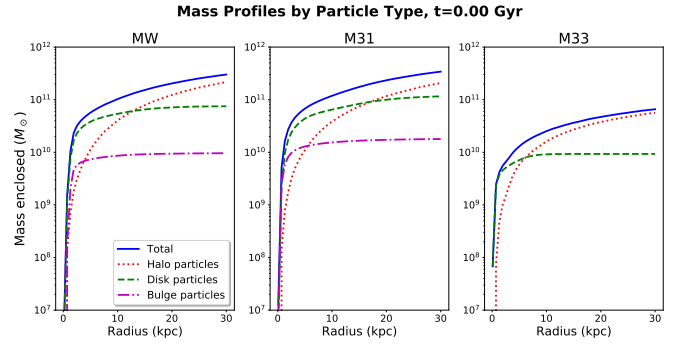


Figure 5. Mass profiles for each galaxy at the current epoch.

then fall steadily at larger radii. With the more diffuse DM halo added, we see the relatively flat overall rotation curves which attracted the attention of astronomers including Zwicky (1933) and Rubin & Ford (1970)

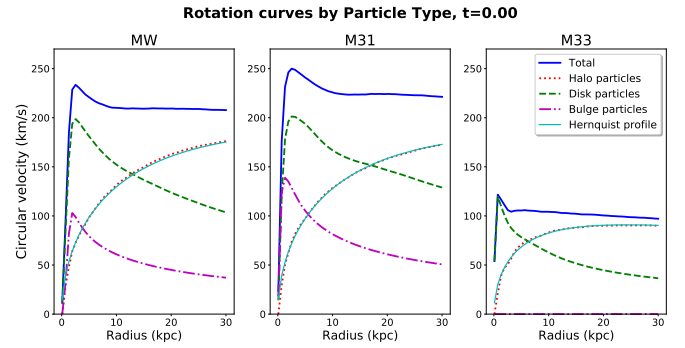


Figure 6. Rotation curves for each galaxy at the current epoch.

TODO set xlim, make y axis log

2.3. Disk particles

2.3.1. Structure

TODO identify the bar?

TODO more on spiral arms

2.3.2. Inclinations

Galactic disks have a well-defined angular momentum vector which is relatively easy to calculate in this type of simulation. Figure 7 shows the angle each makes to the X'-Y' plane over time.

The mutual angle between galactic disks can have a significant impact on how tidal disruption and merger dynamics play out **TODO** ref?. This can be calculated from the vector dot products:

$$\theta = \arccos(\hat{L}_1 \cdot \hat{L}_2)$$

Results for the MW-M31 and M33-M31 pairs are shown in Figure 8. For MW-M31, the angle is largely

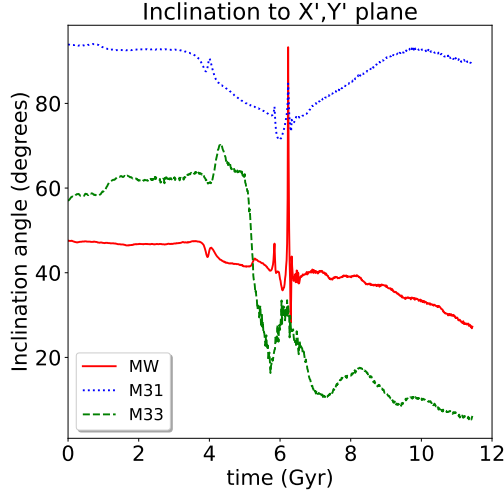


Figure 7. Angular momentum inclination angle to the X',Y' plane for each set of galactic disk particles.

stable until near first pericenter, when tidal forces bring the two disks closer to alignment. This trend continues slowly until near second pericenter. Surprisingly, the angle increases after merger, suggesting some partitioning of particles of different origin within the remnant.

TODO CHECK THIS AGAIN!

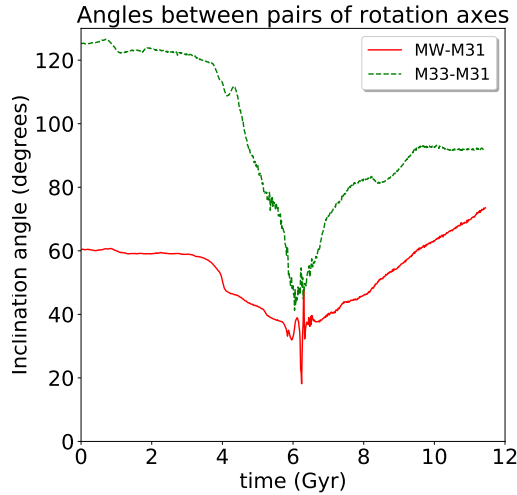


Figure 8. Angular momentum angles between pairs of galaxies.

The large variations in M33-M31 angles are indicative of the extensive tidal disruption of the much smaller M33 galaxy. Details are outside the scope of the present paper.

2.3.3. Velocity dispersion

The changes in velocity dispersion of disk particles originating from each galaxy are shown in Figure 9. The small periodic oscillation seen from the start, especially in M31, appears to be caused by deviations from radial symmetry in the disk: spiral arms and an increasingly prominent bar. Small MW spikes at initial pericenter (around 4 Gyr) and much larger ones at merger (around 6 Gyr) are clearly visible.

M33 is on an irregular, elliptical and decaying orbit about the MW-M31 merger remnant after about 6.5 Gyr. Velocity dispersion appears to peak at intervals. This perhaps corresponds to successive pericenters when M33 experiences maximal tidal disruption, but this will need further analysis.

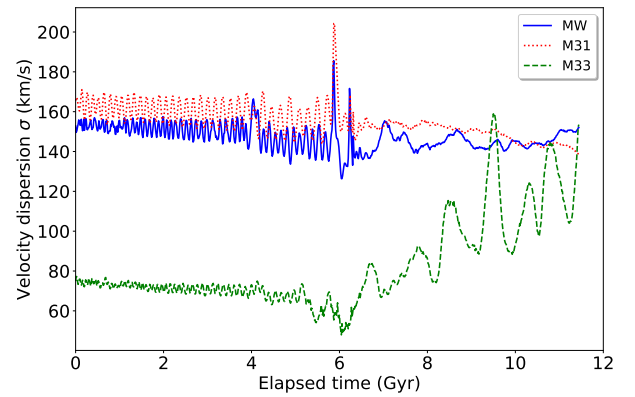


Figure 9. Velocity dispersion of disk particles from each galaxy over time.

2.4. Galactic Bulge

A bulge is present in the MW and M31 but not M33. This region of generally older stars extends further above and below the central plane than disk stars. Kinematics of the bulge are more typical of an elliptical galaxy than a spiral disk.

In a study of elliptical galaxies, de Vaucouleurs showed that surface brightness falls off exponential with radius and approximately as the one-fourth power of radius (de Vaucouleurs 1948). Later work found that this was too restrictive for a wider population of galaxies, so Sérsic generalized the formula to have the inverse exponential n as an additional free parameter (Sérsic 1963):

$$\log_{10} \left(\frac{I(r)}{I_e} \right) = -3.3307 \left[\left(\frac{r}{R_e} \right)^{1/n} - 1 \right]$$

Here R_e is the radius with which half the light is emitted, I_e is the surface brightness at R_e and n is the Sérsic parameter.

This formula is intended for analyzing photographic images and is in terms of light intensity. We have no

brightness data in the current simulation, but for systems with few young blue stars we can assume the mass to light ratio $M/L \sim 1$. This is probably a reasonable approximation for undisturbed bulges and for an elliptical merger remnant long after the collision. R_e is then the radius enclosing half the mass.

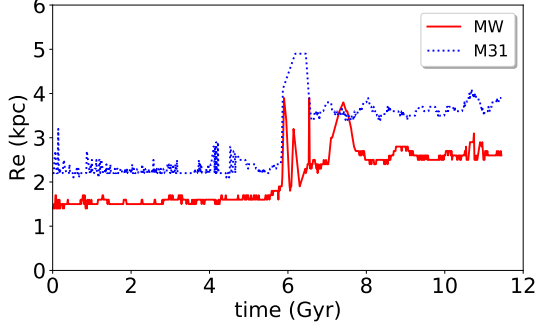


Figure 10. Half-mass radius for bulge particles.

We can see from Figure 10 that for each galaxy the bulge half-mass radius is fairly stable up to the collision and merger of MW and M31. After a period of disturbance, they again become stable at a higher level. The M31 bulge is more diffuse than the MW bulge throughout, and the ex-bulge stars are clearly not randomized in the merger remnant: ex-M31 stars tend towards larger radii than ex-MW stars.

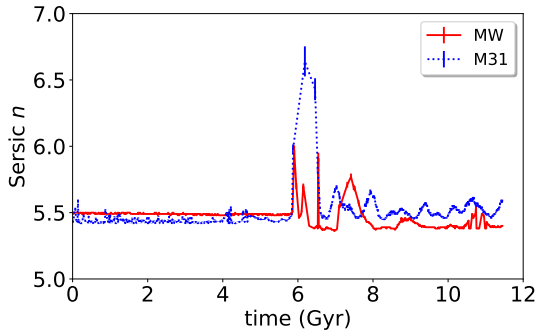


Figure 11. Sérsic n for bulge particles, with 1σ error bars.

The Sérsic parameter n was estimated by a nonlinear least squares fit to the bulge mass profile. As shown in Figure 11 it is fairly constant around 5.5 for any period with meaningful data. The spikes around 6 Gyr should probably be ignored: many values in this collision period are missing, as the least-squares fit failed, and the available data has substantially larger error bars than during stable epochs.

The larger half-mass radius of M31 is reflected in the mass density profile, as shown in Figure 12. MW bulge stars have a higher central peak, M31 bulge stars are

more numerous at larger radii. This is true both early in the simulation, and in the merger remnant at late times. For both galaxy bulge stars, the central peak is less pronounced post-merger.

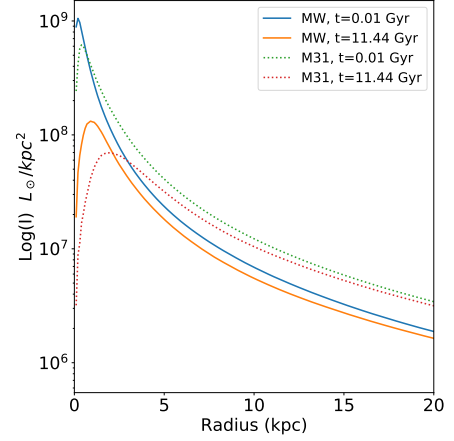


Figure 12. Bulge mass density profile for both galaxies at the beginning and end of the simulation.

The Sérsic fit for both galaxy bulges looks reasonable outside the central density peak, as shown for the MW in Figure 13. The plot for M31 (not included here) is very similar.

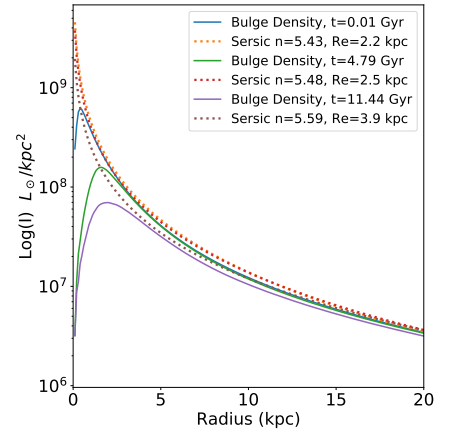


Figure 13. MW bulge mass density profiles and Sérsic best fits. Time points are the beginning, the pre-merger pericenter, and the end of the simulation

2.5. Dark Matter halo

2.5.1. Halo mass profile

Figure 6 also adds a theoretical curve in which the DM halo is fitted by a Hernquist profile (Hernquist 1990). The cumulative mass out to radius r is given by

$$M(r) = M_h \frac{r^2}{(a+r)^2}$$

where M_h is the total mass of halo particles (see Table 2) and a is a scale radius which encloses a quarter of the halo mass. Non-linear least squares fitting, similar to that used for Sérsic profiles in a previous section, gave scale radii of 61.1 kpc for MW and M31, 24.3 kpc for M33 at $t = 0$.

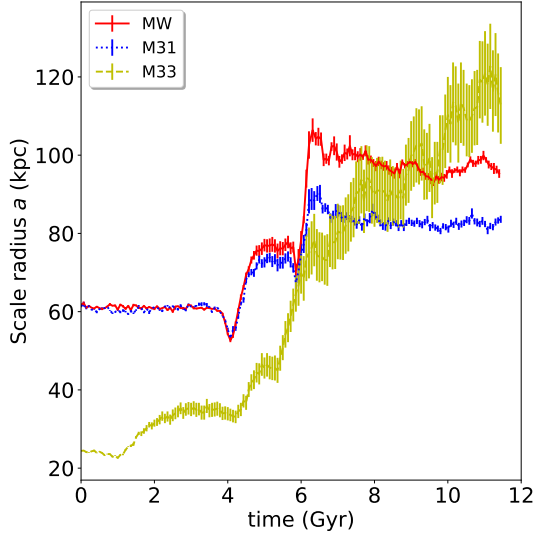


Figure 14. Hernquist scale radius a for DM halo particles originating from each galaxy, with 1σ error bars.

Time evolution of the scale radius a is shown in Figure 14. The MW and M31 remain very similar through first pericenter, then start to diverge with MW particles tending to a larger radius than M31. This becomes most pronounced during and after merger. The dissimilar distribution in the merger remnant will be discussed in a later section.

The scale radius for M33 grows inexorably as the original halo is scattered by tidal forces. Figure 14 also shows the increasingly wide error bars for M33: halo particles for this galaxy are no longer well fitted by a Hernquist profile.

2.5.2. Halo rotation

The specific angular momentum \vec{h} can be calculated from

$$\vec{h} = \frac{\sum_i \vec{r}_i \times m_i \vec{v}_i}{\sum_i m_i}$$

The specific angular momentum for each large galaxy is shown in Figure 15. It appears that both are barely rotating at the current epoch, but spin up rapidly during first pericenter and again around the time of merger, as tidal forces convert orbit angular momentum into spin angular momentum. Differences in the remnant will be discussed in a later section

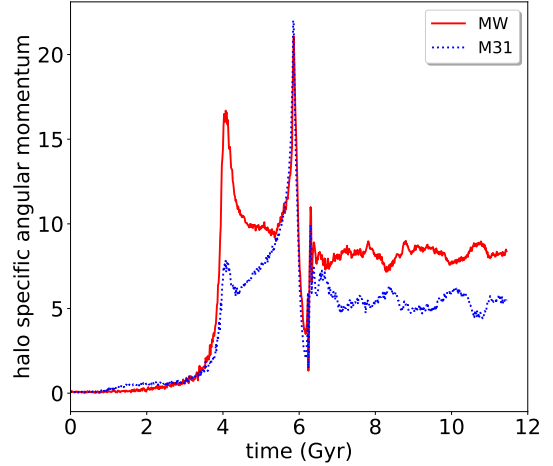


Figure 15. Specific angular momentum for halo particles of each galaxy about its CoM (kpc^2/Myr).

Data for M33 is omitted from Figure 15 for clarity. The spin-up is much more dramatic for this minor galaxy, with peaks approaching $140 \text{ kpc}^2/\text{Myr}$, making it unsuitable to plot on the same axes.

2.6. MW-M31 Close approach

2.6.1. Inclinations

The MW and M31 disks have angular momentum vectors inclined at an angle of 52° to each other shortly before pericenter, making this a prograde approach.

2.6.2. Tidal tails and bridges

The presence of long, symmetrical tails giving some galaxies a distinct ‘S’-shape has been described at least as far back as Zwicky (1955). Some astronomers postulated that these were the result of tidal forces during close, glancing encounters, but this was often contested until a detailed computational study by Toomre & Toomre (1972).

Reviewing a broad range of N-body simulations, Barnes & Hernquist (1992) noted that “such features are clearly *relics* of recent collisions rather than ongoing interactions.” In our simulation, both MW and M31 disks remain near-circular during much of the close approach, but conspicuous tails develop as the centers then move further apart. We also see a more sparsely-populated bridge forming between the galaxies.

To determine the nature and origin of stars in this region, a manual selection was performed as in Figure 16. Stars within the yellow rectangle (left panel) are shown with velocity vectors (center panel) and origin (right panel). Velocities are mostly moderate (mean 195 km/s, range 19–586 km/s), with relatively few stars having high kinetic energy.

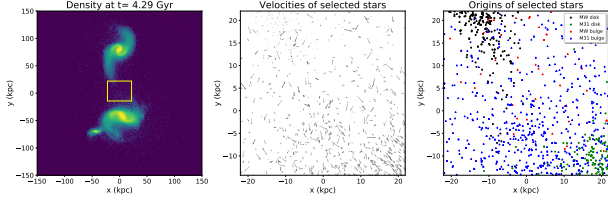


Figure 16. Manual selection of bridge particles at 0.33 Gyr after the first MW-M31 pericenter. The left panel shows stellar surface density and the selected region. The center panel shows velocity vectors for these stars and the right panel shows origin by galaxy and particle type. Orientation is with MW top, M31 bottom and M33 lower left. **TODO** make this page-width in final layout

It appears from the right panel that stars in the tail regions originate in the corresponding disk. The bridge region is more mixed and appears to have a high proportion of former bulge stars. To study this further the coordinate system was transformed to place the large galaxy CoMs on the x -axis at ± 64 kpc, as in Figure 17. It is clear in this view that one MW tail is oriented approximately towards the center of M31.

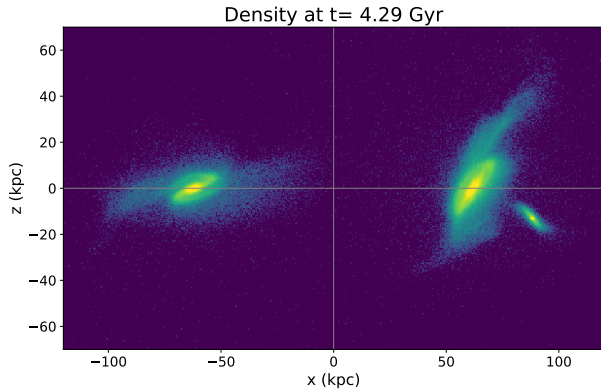


Figure 17. View along the midplane between the galactic centers, MW on the left.

Table 3. Particle counts close to the midplane

	Bulge	Disk	Total
MW	305	1317	1622
M31	1137	4	1141
Total	1442	1321	2763

The different orientations mean that symmetry about the midplane is imperfect, so the “bridge” region was taken as $-20 < x < 30$ kpc. A count of stars in this

region is shown in Table 3. This confirms that the largest populations are MW disk stars (mostly in a relatively dense tail) and M31 bulge stars (more widely dispersed).

TODO identify, trace history, trace fate

TODO Jacobi radius

2.6.3. Mass transfer

Stars are scattered from galaxies even in normal times, and this can be expected to increase significantly during near-misses and collisions. To get a first impression of how many stars and DM particles may end up closer to a different galaxy, we looked at the relative distances of each particle to each of the three galaxy CoMs. It should be emphasized that kinematics is not considered at this stage, so nothing can be said about which particles are gravitationally bound.

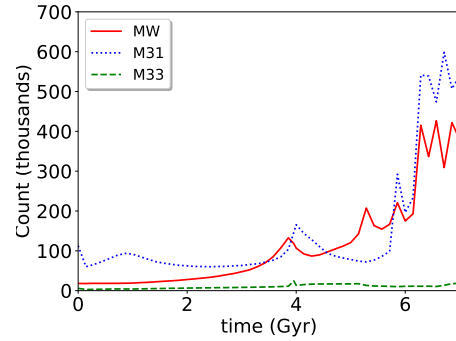


Figure 18. Particles closer to a different CoM.

Figure 18 shows that some particles are far from their notional galaxy even at the start. This increases somewhat during first pericenter around 4 Gyr, then jumps permanently during the second pericenter and merger. The plot cuts off at 7 Gyr because it becomes meaningless to consider the MW/M31 CoMs as separate points post-merger.

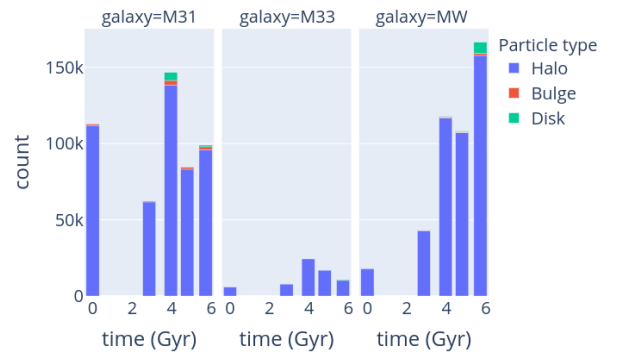


Figure 19. Particles closer to a different CoM.

Figure 19 looks at a few timepoints by particle type, showing that the overwhelming majority of these particles are from the DM halo. This is unremarkable, given the prevalence of these particles at large radii and their correspondingly weak gravitational binding.

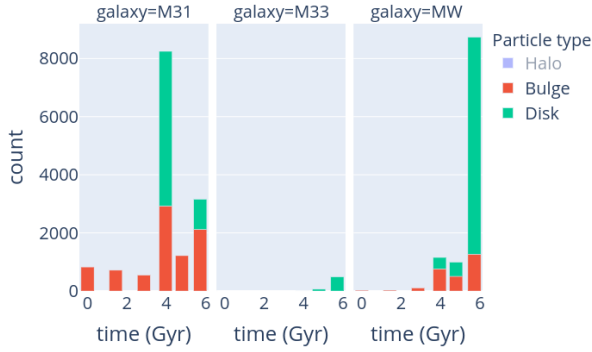


Figure 20. Luminous particles closer to a different CoM (DM halo hidden).

To focus on the baryonic matter, Figure 20 hides the DM halo and expands the y -axis to show only bulge and disk particles. There are significant numbers of M31 bulge particles at all timepoints, mostly reflecting the proximity of M33. The last three bars on each panel correspond to first pericenter, apocenter, and second pericenter. M31 disk particle numbers jump at first pericenter but these apparently remain bound to the original galaxy: virtually all return to M31 before apocenter.

2.7. MW-M31 merger

After second pericenter, the MW and M31 never fully separate and eventually merge. Their mass ratio is 1:1.6 for stellar matter and 1:1 when the DM halo is included. This is thus a ‘major merger’ in the terminology of [TODO](#) ref?. A 1:1 mass ratio has been reported ([Boylan-Kolchin et al. 2008](#); [Ji et al. 2014](#)) to lead to the shortest coalescence time.

The 3D trajectories are complex, but Figures 21 and 22 are snapshots which attempts to show this. The MW CoM is always at the origin and the points show the M31 CoM at regular 14.3 Myr intervals. First pericenter is at upper left (outer), apocenter at the bottom, second pericenter in the tight reversal at upper left. The path is smooth up to 6.1 Gyr then becomes more chaotic.

[TODO](#) changes in mass profile

2.7.1. Inclinations

[TODO](#) Relative rotation axes of disks – prograde?

2.8. MW-M31 merger remnant

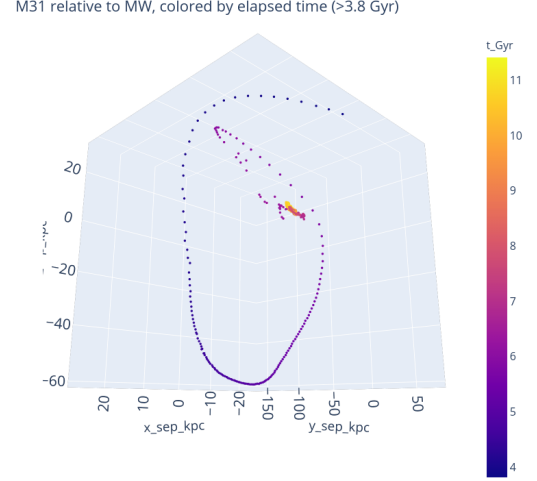


Figure 21. Approach and merger in a MW-centric coordinate frame. Points are spaced at 14.3 Myr intervals.).

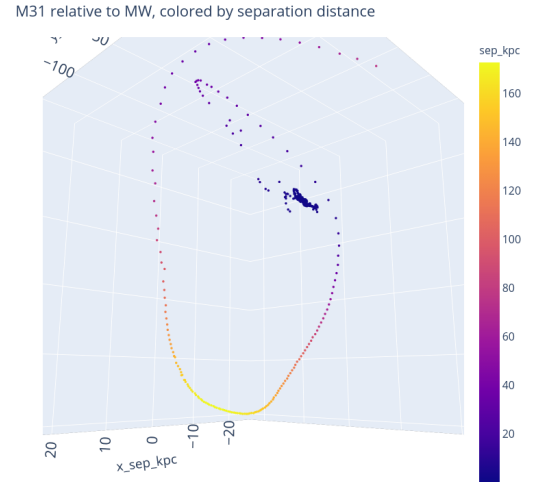


Figure 22. Approach and merger. Similar to Figure 21 except the color coding is by separation.

2.8.1. Remnant shape

[TODO](#) how to get principal axes? boxiness?

We can expect the remnant to settle over time into a triaxial ellipsoid [TODO](#) ref?. These are superficially rather featureless, as in Figure 23.

In observational astronomy it would be usual to fit parameters to surface brightness contours. That would also be possible for the simulation, but for a highly-determined system for which we know the mass and position of every particle there are other options.

If we combine all the baryonic matter (disk and bulge) from both MW and M31, there are 1.12×10^6 particles

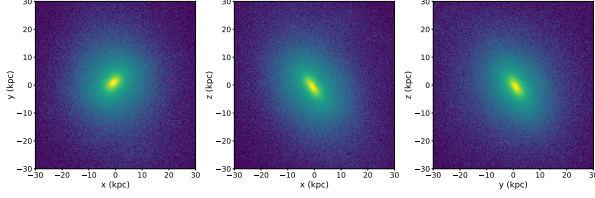


Figure 23. Luminous star density of the MW-M31 remnant in three orthogonal projections.

to consider. In the original coordinates, the moment of inertia tensor is symmetrical, 3×3 :

$$I = \begin{bmatrix} I_{xx} & I_{xy} & I_{xz} \\ I_{yx} & I_{yy} & I_{yz} \\ I_{zx} & I_{zy} & I_{zz} \end{bmatrix}$$

$$I_{total} \approx \begin{bmatrix} 2.44e+04 & 2.55e+02 & 1.43e+03 \\ 2.55e+02 & 1.91e+04 & -1.71e+01 \\ 1.43e+03 & -1.71e+01 & 2.22e+04 \end{bmatrix}$$

The orientation is arbitrary at this stage. To get principal axes we need the eigenvalues and eigenvectors of I .

The eigenvalues give the moments of inertia about the principal axes, in arbitrary units scaled such that $A = 1$:

$$a = 1.0, b = 0.85, c = 0.79$$

The luminous ellipsoid is thus triaxial (low symmetry).

The eigenvectors give an orthonormal coordinate system oriented along the principal axes:

$$\begin{aligned} \hat{v}_a &= \langle +0.070, -0.996, -0.050 \rangle \\ \hat{v}_b &= \langle -0.423, -0.075, +0.903 \rangle \\ \hat{v}_c &= \langle -0.904, -0.042, -0.426 \rangle \end{aligned}$$

The moment of inertia of an ellipsoid with semi-major axes a, b, c is $A = k(b^2 + c^2)$ where k is a constant that depends on total mass. Other axes have the same form by symmetry. Solving for a, b, c and normalizing gives:

$$a = 1.0, \quad b = 0.94, \quad c = 0.77$$

So the minor axis is significantly smaller than the other two: the ellipsoid is approximately prolate.

This was repeated for each subgroup by particle origin. The numbers involved are shown in Table 3.

The relative axis lengths are shown in Table 4. All subgroups are triaxial, but ex-MW disk particles are distinctive in retaining a particularly flattened distribution.

Table 3. Counts of particles by origin (thousands)

Galaxy	Bulge	Disk	All
M31	95	600	695
MW	50	375	425
All	145	975	1120

Table 4. Relative size of axes by particle origin

Galaxy	a	b	c
total	1.0	0.94	0.77
MW disk	1.0	0.90	0.53
MW bulge	1.0	0.89	0.76
M31 disk	1.0	0.88	0.71
M31 bulge	1.0	0.78	0.71

The mutual inclination angles of the major axes are shown in Table 5. Again, the former disk particles are seen to retain a distinctive structure. Clearly this collision and a single merger is not sufficient to randomize stars within the remnant **TODO** refs?. Also, this is consistent with the understanding that relaxation times are very long in collisionless systems on the scale of elliptical galaxies (Binney & Tremaine 2008, Section 1.2)

Table 5. Mutual inclination angles of major axis by particle origin (degrees). Suffix indicates source: **disk/bulge**.

	Total	MWd	MWb	M31d	M31b
total	–	45.9	15.0	83.2	19.4
MWd	45.9	–	46.7	41.4	60.6
MWb	15.0	46.7	–	87.6	32.4
M31d	83.2	41.4	87.6	–	89.0
M31b	19.4	60.6	32.4	89.0	–

TODO Overlay this on contour fit to check it
TODO redo this for various radii cutoffs

2.8.2. Remnant mass distribution

The mass profile for each type of particle and overall is shown in Figure 24. This is similar to Figure 5, except that the radius now extends out to 100 kpc.

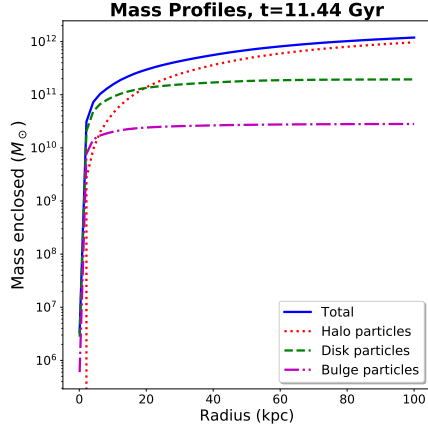


Figure 24. Mass profiles of the remnant by particle type.

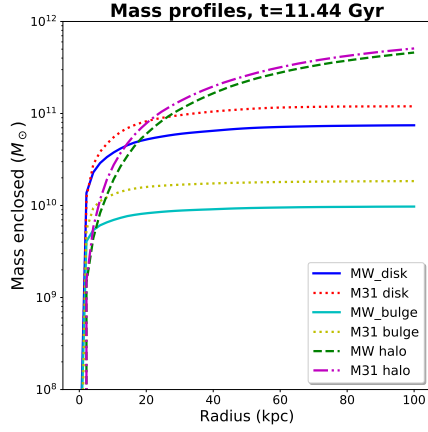


Figure 25. Mass profiles of the remnant by origin.

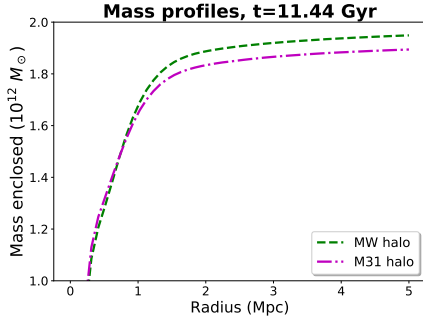


Figure 26. Mass profiles of the outer part of the remnant halo.

Previous sections have shown that MW and M31 particles remain somewhat distinct after merger. Figure 25 compares their mass profiles. For baryonic particles, ex-M31 masses are higher than ex-MW at most radii, reflecting the higher baryonic mass fraction in M31. The opposite effect might be expected for the DM halo, whose total mass was significantly higher in the

MW (Table 2), but this is not seen out to 100 kpc. Figure 26 suggests we have to go almost 1 Mpc out before MW particles become the largest halo component.

TODO Would be better to plot $\rho(r)$

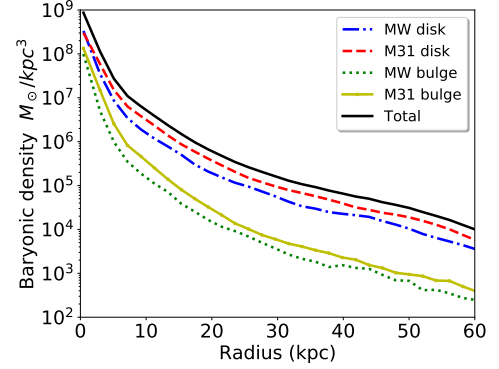


Figure 27. Spherically-averaged density profiles of the remnant luminous matter by origin.

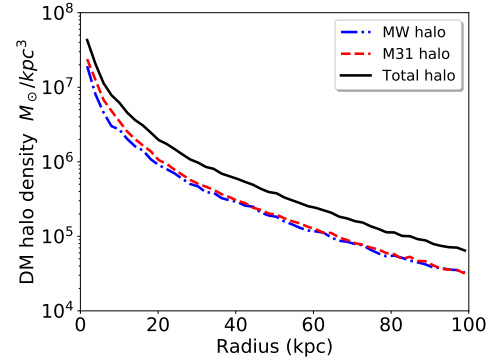


Figure 28. Spherically-averaged density profiles of the remnant halo by origin. Note the expanded x -axis relative to Figure 27

Figure 29 shows Sérsic fits to the surface brightness profile (assuming $M/L \sim 1$).

The mass profile of DM particles in the remnant halo is well fit by a Hernquist profile, but there are some differences depending on origin as shown in Table 6

Table 6. Best-fit Hernquist a for remnant halo

Origin	$a \pm \text{StdDev (kpc)}$
total	84.5 ± 0.5
ex-MW	95.2 ± 1.4
ex-M31	82.3 ± 0.9

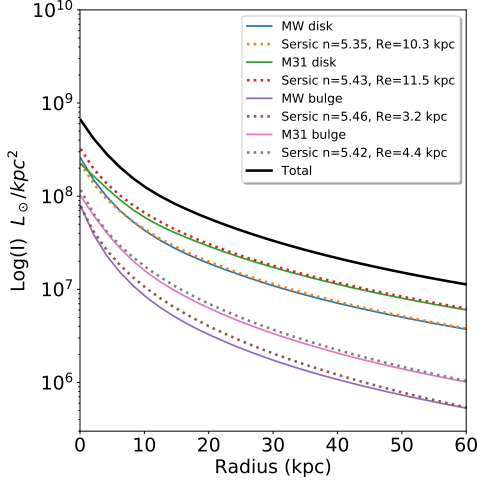


Figure 29. Surface brightness profiles of the remnant by origin.

For comparison, the values at $t = 0$ were 61.6 ± 0.5 kpc for the MW and 61.4 ± 0.2 kpc for M31. The overall time-dependence of Hernquist radii was shown in Figure 14.

2.8.3. Remnant rotational kinematics

The specific angular momentum \vec{h} was calculated for all the particles in the merger remnant and various subsets, as shown in Table 7

Table 7. Specific angular momentum components for the merger remnant at $t=11.44$ Gyr ($\text{kpc}^2 / \text{Myr}$)

	\hat{h}_x	\hat{h}_y	\hat{h}_z	$ h $
total	0.64	0.03	-0.77	12.77
MW disk	0.65	-0.13	-0.75	6.43
M31 disk	0.53	-0.21	-0.82	6.28
MW bulge	0.62	-0.05	-0.78	6.80
M31 bulge	0.61	-0.12	-0.78	6.22
MW halo	0.66	0.09	-0.74	16.89
M31 halo	0.60	-0.08	-0.80	9.42

A previous section showed that the remnant is elliptical and particles of different orientation are oriented very differently (Table 5). When this analysis is repeated for the angular momentum vectors the mutual inclination angles are non-zero but generally quite small, as shown in Table 8.

TODO Is it a fast or slow rotator?

For the aggregate of all DM particles in the remnant at this time, the angular momentum vector has orienta-

Table 8. Mutual inclination angles for rotation vectors in the merger remnant at $t=11.44$ Gyr (degrees)

	total	MWd	M31d	MWb	M31b	MWh	M31h
total	—	9.0	15.5	4.5	8.9	4.2	6.9
MWd	9.0	—	9.2	5.4	3.2	12.7	4.9
M31d	15.5	9.2	—	11.0	7.0	19.7	8.7
MWb	4.5	5.4	11.0	—	4.5	8.7	2.4
M31d	8.9	3.2	7.0	4.5	—	13.1	2.7
MWh	4.2	12.7	19.7	8.7	13.1	—	11.1
M31h	6.9	4.9	8.7	2.4	2.7	11.1	—

tion $\hat{h} = \langle 0.64, 0.03, -0.76 \rangle$, almost identical to the total for all particles (baryonic + DM) in the remnant. The magnitude $|h| = 13.15 \text{ kpc}^2/\text{Myr}$ is more than two orders of magnitude higher than the values for the individual galaxies about their respective CoM at the current epoch.

We showed in Figure 15 that halo angular momentum mostly arises from tidal forces during close approach and merger, and in Figure 14 that MW halo particles subsequently have a significantly larger scale radius than M31 halo particles. As specific angular momentum is a product of radius and tangential velocity, it seems reasonable that we see a higher value for ex-MW Dark Matter when it tends to be at larger radius.

TODO fix section on phase diagrams

Baryonic particles in the merger remnant have a small net angular momentum, and we can rotate the coordinate system to align this vector with the z -axis. However, the phase diagrams in Figure 30 show that velocities are mostly randomly distributed and few of the particles show much asymmetry.

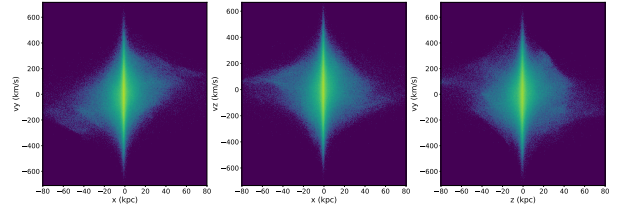


Figure 30. Phase diagrams of the MW-M31 remnant, orthogonal views.

3. DISCUSSION AND CONCLUSIONS

TODO add some!

4. ACKNOWLEDGMENTS

The author is grateful to Prof. Gurtina Besla for teaching the class which this paper is based on and allowing this rather geriatric student to participate, as well as providing all the raw data from the earlier simulation. Also to Rixin Li for valuable coding advice.

This work relied on a range of open-source software packages, many of them sponsored by NumFOCUS³ for the benefit of us all:

- NumPy (van der Walt et al. 2011)
- Matplotlib (Hunter 2007)

- pandas (pandas development team 2020; Wes McKinney 2010)
- Astropy (Astropy Collaboration et al. 2013)
- SciPy (Virtanen et al. 2020)
- IPython (Perez & Granger 2007)
- Jupyter (Kluyver et al. 2016)
- conda-forge⁴

Additionally, mpl-scatter-density⁵ and Plotly⁶ were used in preparing the figures.

REFERENCES

- Astropy Collaboration, Robitaille, T. P., Tollerud, E. J., et al. 2013, *A&A*, 558, A33, doi: [10.1051/0004-6361/201322068](https://doi.org/10.1051/0004-6361/201322068)
- Barnes, J. E., & Hernquist, L. 1992, *Annual Review of Astronomy and Astrophysics*, 30, 705, doi: [10.1146/annurev.aa.30.090192.003421](https://doi.org/10.1146/annurev.aa.30.090192.003421)
- Binney, J., & Tremaine, S. 2008, *Galactic Dynamics: Second Edition*, by James Binney and Scott Tremaine. ISBN 978-0-691-13026-2 (HB). Published by Princeton University Press, Princeton, NJ USA, 2008. <http://adsabs.harvard.edu/abs/2008gady.book.....B>
- Boylan-Kolchin, M., Ma, C.-P., & Quataert, E. 2008, *Monthly Notices of the Royal Astronomical Society*, 383, 93, doi: [10.1111/j.1365-2966.2007.12530.x](https://doi.org/10.1111/j.1365-2966.2007.12530.x)
- Brown, A. G. A., Vallenari, A., Prusti, T., et al. 2018, *Astronomy & Astrophysics*, 616, A1, doi: [10.1051/0004-6361/201833051](https://doi.org/10.1051/0004-6361/201833051)
- de Vaucouleurs, G. 1948, *Annales d'Astrophysique*, 11, 247. <http://adsabs.harvard.edu/abs/1948AnAp...11..247D>
- Hernquist, L. 1990, *The Astrophysical Journal*, 356, 359, doi: [10.1086/168845](https://doi.org/10.1086/168845)
- Hunter, J. D. 2007, *Computing in Science & Engineering*, 9, 90, doi: [10.1109/MCSE.2007.55](https://doi.org/10.1109/MCSE.2007.55)
- Ji, I., Peirani, S., & Yi, S. K. 2014, *Astronomy & Astrophysics*, 566, A97, doi: [10.1051/0004-6361/201423530](https://doi.org/10.1051/0004-6361/201423530)
- Kluyver, T., Ragan-Kelley, B., Pérez, F., et al. 2016, in *Positioning and Power in Academic Publishing: Players, Agents and Agendas*, ed. F. Loizides & B. Schmidt, IOS Press, 87 – 90
- Marel, R. P. v. d., Besla, G., Cox, T. J., Sohn, S. T., & Anderson, J. 2012a, *The Astrophysical Journal*, 753, 9, doi: [10.1088/0004-637X/753/1/9](https://doi.org/10.1088/0004-637X/753/1/9)
- Marel, R. P. v. d., Fardal, M., Besla, G., et al. 2012b, *The Astrophysical Journal*, 753, 8, doi: [10.1088/0004-637X/753/1/8](https://doi.org/10.1088/0004-637X/753/1/8)
- Marel, R. P. v. d., Fardal, M. A., Sohn, S. T., et al. 2019, *The Astrophysical Journal*, 872, 24, doi: [10.3847/1538-4357/ab001b](https://doi.org/10.3847/1538-4357/ab001b)
- Mo, H., van den Bosch, F. C., & White, S. 2010, *Galaxy Formation and Evolution*, by Houjun Mo, Frank van den Bosch, Simon White, Cambridge, UK: Cambridge University Press, 2010. <http://adsabs.harvard.edu/abs/2010gfe..book.....M>
- pandas development team, T. 2020, pandas-dev/pandas: Pandas, latest, Zenodo, doi: [10.5281/zenodo.3509134](https://doi.org/10.5281/zenodo.3509134)
- Perez, F., & Granger, B. E. 2007, *Computing in Science & Engineering*, 9, 21, doi: [10.1109/MCSE.2007.53](https://doi.org/10.1109/MCSE.2007.53)
- Rubin, V. C., & Ford, Jr., W. K. 1970, *The Astrophysical Journal*, 159, 379, doi: [10.1086/150317](https://doi.org/10.1086/150317)
- Sérsic, J. L. 1963, *Boletín de la Asociación Argentina de Astronomía La Plata Argentina*, 6, 41. <http://adsabs.harvard.edu/abs/1963BAAA....6...41S>
- Toomre, A., & Toomre, J. 1972, *The Astrophysical Journal*, 178, 623, doi: [10.1086/151823](https://doi.org/10.1086/151823)
- van der Walt, S., Colbert, S. C., & Varoquaux, G. 2011, *Computing in Science & Engineering*, 13, 22, doi: [10.1109/MCSE.2011.37](https://doi.org/10.1109/MCSE.2011.37)
- Virtanen, P., Gommers, R., Oliphant, T. E., et al. 2020, *Nature Methods*, doi: <https://doi.org/10.1038/s41592-019-0686-2>
- Wes McKinney. 2010, in *Proceedings of the 9th Python in Science Conference*, ed. Stéfan van der Walt & Jarrod Millman, 56 – 61, doi: [10.25080/Majora-92bf1922-00a](https://doi.org/10.25080/Majora-92bf1922-00a)
- Zwicky, F. 1933, *Helvetica Physica Acta*, 6, 110. <http://adsabs.harvard.edu/abs/1933AcHPh...6..110Z>

³ <https://numfocus.org/>

⁴ <https://conda-forge.org/>

⁵ <https://github.com/astrofrog/mpl-scatter-density>

⁶ <https://plotly.com/python/>

- . 1955, Publications of the Astronomical Society of the Pacific, 67, 232, doi: [10.1086/126807](https://doi.org/10.1086/126807)